International Journal of Fatigue 151 (2021) 106384

Contents lists available at ScienceDirect

International Journal of Fatigue

journal homepage: www.elsevier.com/locate/ijfatigue

Establishing specimen property to part performance relationships for laser beam powder bed fusion additive manufacturing

Arash Soltani-Tehrani [a,b], Rakish Shrestha [a,b], Nam Phan [c], Mohsen Seifi [d,e], Nima Shamsaei [a,b,*]

[a] National Center for Additive Manufacturing Excellence (NCAME), Auburn University, Auburn, AL 36849, USA
[b] Department of Mechanical Engineering, Auburn University, Auburn, AL 36849, USA
[c] Structures Division, U.S. Naval Air System Command (NAVAIR), Patuxent River, MD 20670, USA
[d] Department of Material Science & Engineering, Case Western Reserve University, Cleveland, OH 44106, USA
[e] ASTM International, Washington, DC 20036, USA

ARTICLE INFO

Keywords:
Additive manufacturing
Laser beam powder bed fusion (LB-PBF)
Process parameters
Melt pool
Porosity
Fatigue behavior

ABSTRACT

This study investigates the possibility of correlating specimen property to part performance for laser beam powder bed fusion (LB-PBF) additive manufacturing by altering the process parameters in order to create similar thermal histories experienced during fabrication. In particular, the effects of altering scanning speed on LB-PBF 17-4 precipitation hardening (PH) stainless steel (SS) parts with different geometries on the thermal history, as well as the resultant defect formation, microstructure, and fatigue behavior are studied. It was found that parts with different geometries, all fabricated using the same manufacturer recommended process parameters, exhibited different fatigue strengths, which challenges the specimen property to part performance correlation. Melt pool analysis revealed that altering scanning speed can affect the melt pool characteristics including its depth and overlap depth. Increasing the input energy within the process window, by decreasing the scanning speed during fabrication, was seen to result in deeper melt pools and melt pool overlaps, and consequently, less volumetric defects, specifically lack of fusion, in the material. Therefore, the scanning speed was adjusted for different geometries to result in similar melt pool characteristics, as an indicator of the thermal history experienced during fabrication, which also resulted in these parts having similar porosity. Accordingly, fatigue lives of parts fabricated with adjusted process parameters were observed to be within a similar range. While many other factors may be involved, the findings of this research indicate that maintaining a similar thermal history by altering the process parameters is critical in establishing reliable relationships between specimen property and part performance in additive manufacturing.

1. Introduction

Additive manufacturing (AM) has enabled the possibility of fabricating parts with complex geometries, which may not be feasible through subtractive manufacturing methods. However, at the current stage of AM technologies, the formation of volumetric defects such as lack of fusion (LoF), keyhole, and entrapped-gas pores is inevitable. The creation of these defects is mainly governed by the melt pool morphology, which in turn is affected by the thermal history experienced by a part during fabrication. The variations in thermal history can primarily be affected by the process parameters (e.g. laser power, scanning speed, hatch spacing, layer thickness, etc.) [1–3]; however, the design parameters (e.g. part size and geometry, layer orientation, etc.) may also influence the thermal history [4–11]. Since the existence of volumetric defects can considerably decrease the fatigue resistance of additively manufactured (AM) parts as compared to the wrought counterparts, an in-depth understanding of the effects of design parameters on the formation and distribution of volumetric defects is required, which can contribute toward qualification and certification of AM materials and parts [5,12–14].

Few studies have been conducted on the effects of part geometry and size on the thermal history, and the resultant defect formation and fatigue performance. It has been shown that the thermal history in parts with different geometries or even at different locations within a part can be different during the AM process [5,9,15,16]. Shrestha et al. [5] showed that the distribution and size of entrapped-gas pores in laser beam powder bed fusion (LB-PBF) 17-4 precipitation hardening (PH) stainless steel (SS) parts with different geometries can vary. In their study, three different geometries including oversized cylindrical dog-

* Corresponding author. Tel.: +1 (334) 844-4839.
E-mail address: shamsaei@auburn.edu (N. Shamsaei).

https://doi.org/10.1016/j.ijfatigue.2021.106384
Received 16 March 2021; Received in revised form 14 May 2021; Accepted 7 June 2021
Available online 10 June 2021

Nomenclature

$2N_f$	Reversals to failure
$DB7.5^-$	Dog-bone parts with 7.5% lower scanning speed
$DB10^-$	Dog-bone parts with 10% lower scanning speed
$DB15^-$	Dog-bone parts with 15% lower scanning speed
$D_{equivalent}$	Equivalent defect size based on Murakami's approach
d_p	Melt pool depth
d_o	Overlap depth between consecutive melt pools
$LB7.5^+$	Large Block parts with 7.5% higher scanning speed
$LB10^+$	Large Block parts with 10% higher scanning speed
$LB20^+$	Large Block parts with 20% higher scanning speed
R_ε	Ratio of minimum to maximum strain
R_a	Arithmetical mean height of the profiled line
t_L	Layer thickness
ε_a	Strain amplitude

Abbreviation

AM	Additive manufacturing/Additively manufactured
CA	Condition A
CT	Computed tomography
DB	Dog-bone
EB-PBF	Electron beam powder bed fusion
HIP	Hot isostatic pressing
LB	Large block
LB-PBF	Laser beam powder bed fusion
LoF	Lack of fusion
PH	Precipitation hardening
SB	Small block
SS	Stainless steel

bone parts with 7 mm diameter, small and large square blocks with 12 × 12 mm^2, and 25 × 25 mm^2 cross-sections were fabricated. Shallower melt pools were observed in the oversized dog-bone parts followed by small blocks, while the deepest melt pools were observed in the large blocks. This variation in the melt pool size was attributed to the different solidification rates in parts with different geometries, which was the fastest in dog-bones and the slowest in large blocks.

In addition, the higher solidification rate in dog-bone parts resulted in a larger and a higher number of defects as compared to the large blocks, which had relatively lower and smaller sized defects [5]. Under uniaxial strain-controlled cyclic loading conditions, fatigue specimens obtained by machining the large square blocks showed better fatigue performance, while the shortest fatigue lives were reported for the specimens acquired from oversized dog-bone parts. Lower fatigue resistance of oversized dog-bone specimens was ascribed to the presence of larger and the greater number of pores [5]. The findings of this study highlighted the importance of adjusting the input energy density and the resulting solidification rates in parts with different geometries. As the input energy density is directly influenced by the employed process parameters including, laser power, scanning speed, hatch spacing, and layer thickness [17], altering the process parameters may be an effective way to change the thermal history experienced in each part during fabrication.

Numerous studies have been performed to investigate the effects of process parameters on the resultant solidification rate by looking into the melt pool morphology and defect formation mechanisms [17–31]. In these studies, variations in the melt pool morphology and size distribution of defects were attributed to different input energy densities as they affect the solidification rate. For instance, Li and Gu [18] reported that the solidification rate during the LB-PBF process of AlSi10Mg can be decreased by increasing the input energy density. Consequently, larger melt pools, better metallurgical bonding, and ultimately decreased LoF defects were observed in the parts as a result of increased laser power and decreased scanning speed, within the conduction regime. A single-track experiment conducted by Makoana et al. [32] on 17-4 PH SS, fabricated using an EOS M280 LB-PBF machine, also revealed that increasing laser power or decreasing scanning speed can increase the melt pool size.

Gong et al. [17] illustrated that using very high scanning speeds and low laser powers in the fabrication of Ti-6Al-4V parts via LB-PBF or electron beam powder bed fusion (EB-PBF) can give low input energy densities, which are not sufficient to completely melt the material. In such conditions, there is no adequate overlap either between the melt pools of subsequent layers or between the adjacent hatch lines within the same layer, resulting in irregularly-shaped LoF defects. Cunningham et al. [20] reported similar observations on the formation of LoF defects in LB-PBF Ti-6Al-4V parts, which was attributed to the inadequate overlap between the melt pools of the adjacent scan tracks. Additionally, it was shown that using high laser powers along with low scanning speeds can yield to the formation of comparably deeper melt pools, and consequently, keyhole pores [20].

Similar observations have been reported for the LB-PBF 316L SS parts [28]. It was indicated in Ref. [28] that increasing the scanning speed, while keeping the laser power constant, or decreasing the laser power at constant scanning speeds can considerably decrease the melt pool depth. Moreover, increasing the scanning speed was found to noticeably decrease the density of the as-fabricated parts. However, when higher laser powers were used, less variation in part density was observed by the increase in scanning speed. Choo et al. [31] investigated the melt pool morphology and defect formation in LB-PBF 316L SS parts fabricated with different laser powers and a constant scanning speed (i.e. 300 mm/s). It was shown that increasing the laser power from 200 to 380 W can decrease the solidification rate almost by the factor of eight. Consequently, larger melt pools, as well as smaller and fewer pores were observed when higher laser powers were used during fabrication.

It was illustrated that design factors such as part size and shape as well as process parameters can remarkably affect the thermal history experienced during the LB-PBF process. This variation in thermal history can give rise to differences in the defect formation and distribution, and ultimately, affect the fatigue performance of the part [5]. Therefore, understanding the effects of design and process parameters on the fatigue behavior of AM parts is of great importance before these parts can be used in applications where they are under dynamic cyclic loads. Such an understanding is also crucial in correlating specimen property to part performance and enabling the design of AM parts based on material's data generated in the laboratory from specimen testing.

In the present study, process parameters are altered to fabricate LB-PBF 17-4 PH SS parts with different geometries in an attempt to maintain a similar thermal history, defect size distribution, and consequently, fatigue resistance among all. This is a major step towards establishing specimen property to part performance relationships in AM and enabling the use of generated material's data in the laboratory utilizing standard specimens to design and qualify AM parts. Following the introduction, the experimental procedure describing the material and part fabrication process, fatigue testing, and microstructural and fractography analyses are presented. The relationships among the melt pool characteristics, defect formation, and the resulting fatigue lives are then presented and discussed. Finally, some conclusions are made based on the presented experimental results and discussions. Although this study is mainly focused on experimental observations, any means of analytical evaluations, thermal simulations, or in-situ monitoring methods are exceedingly recommended, which can contribute toward property-performance correlations [33–36].

Table 1
Major process parameters utilized for fabrication of LB-PBF 17-4 PH SS parts using an EOS M290.

	Scanning speed (mm/s)	Laser power (W)	Hatching space (μm)	Layer thickness (μm)	Stripe width (mm)
SB Default	755.5				
DB7.5^{-}	698.8				
DB10^{-}	680.0				
DB15^{-}	642.2	220	100	40	100
LB7.5^{+}	812.2				
LB10^{+}	831.1				
LB20^{+}	906.6				

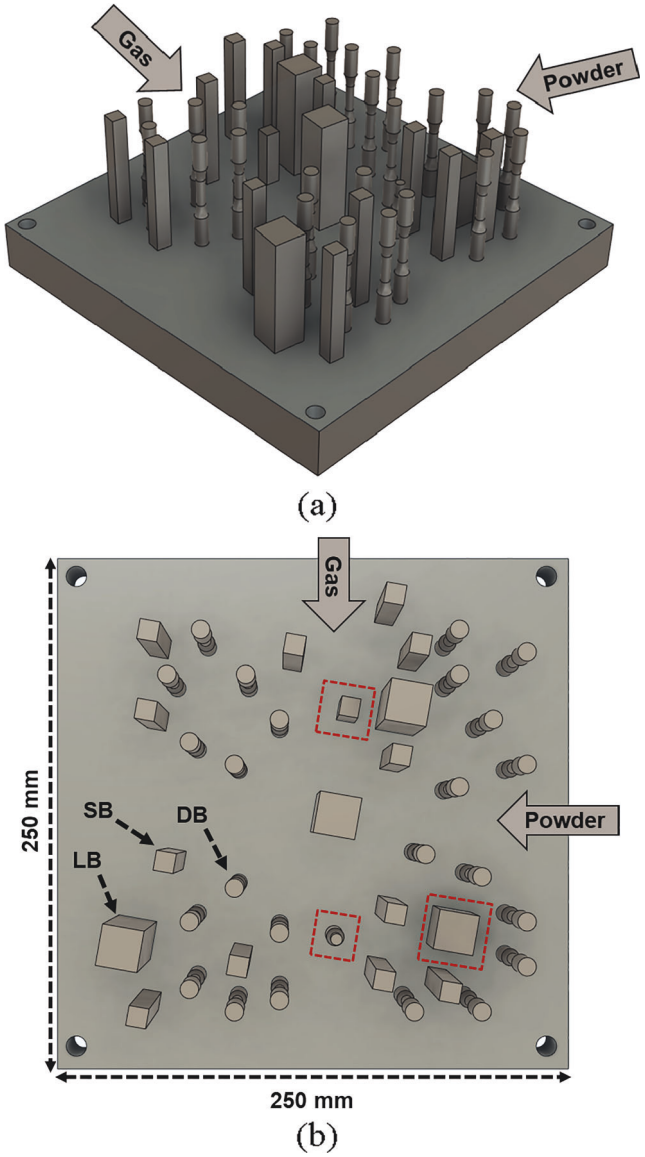

Fig. 1. (a) Isometric and (b) top views of the build layout used to fabricate oversized dog-bone (DB) parts with 7 mm gage diameter and 90 mm height, 12 × 12 × 90 mm^3 small blocks (SB), and 25 × 25 × 90 mm^3 large blocks (LB) in an EOS M290 machine under nitrogen environment and from argon-atomized 17-4 PH SS powder. The half-built melt pool specimens are indicated with red dashed squares. (For interpretation of the references to colour in this figure legend, the reader is referred to the web version of this article.)

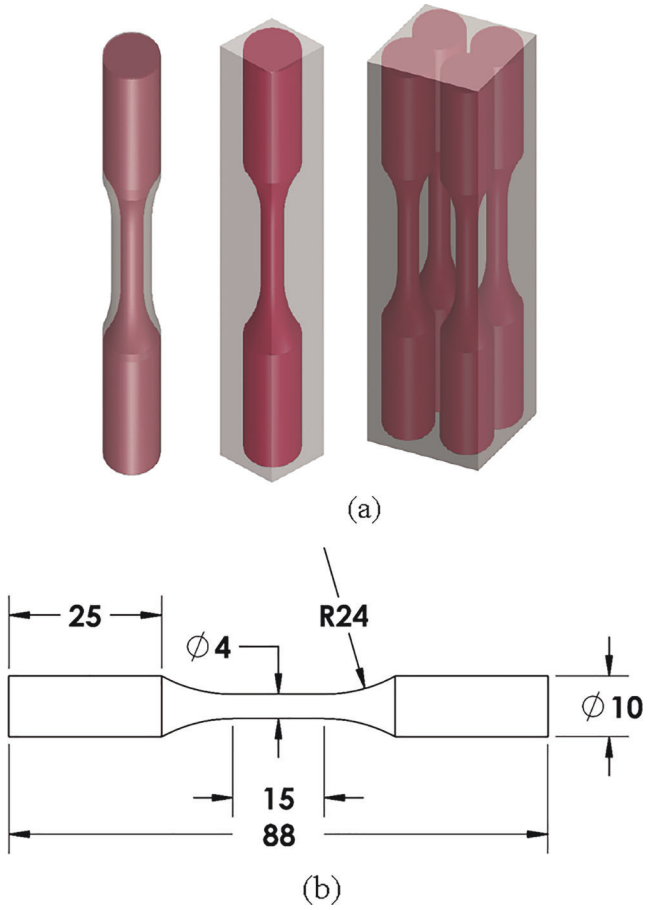

Fig. 2. (a) Schematic illustration of oversized dog-bone (DB), small block (SB), and large block (LB) specimens which were further machined to the geometry of fatigue specimens with uniform gage section shown in (b) [5]. All dimensions are in mm.

2. Experimental procedures

2.1. Material and part fabrication

Argon atomized 17-4 PH SS powder from Carpenter Technology with a particle size distribution of 15–45 μm and the chemical composition reported in Ref. [5] was utilized to fabricate all parts in this study. It is also important to mention that the current study is the continuation of the work already published in Ref. [5]. In the previous study [5], the fatigue lives of 17-4 PH SS parts were seen to be affected by the part geometry, which was related to its effect on the thermal history experienced by each part during the fabrication. Three different geometries were designed to introduce variation in thermal history during fabrication, which included an oversized dog-bone part with a 7 mm diameter and two different square blocks with 12 × 12 mm^2 (small block) and 25 × 25 mm^2 (large block) cross-sections. Since all of the parts with

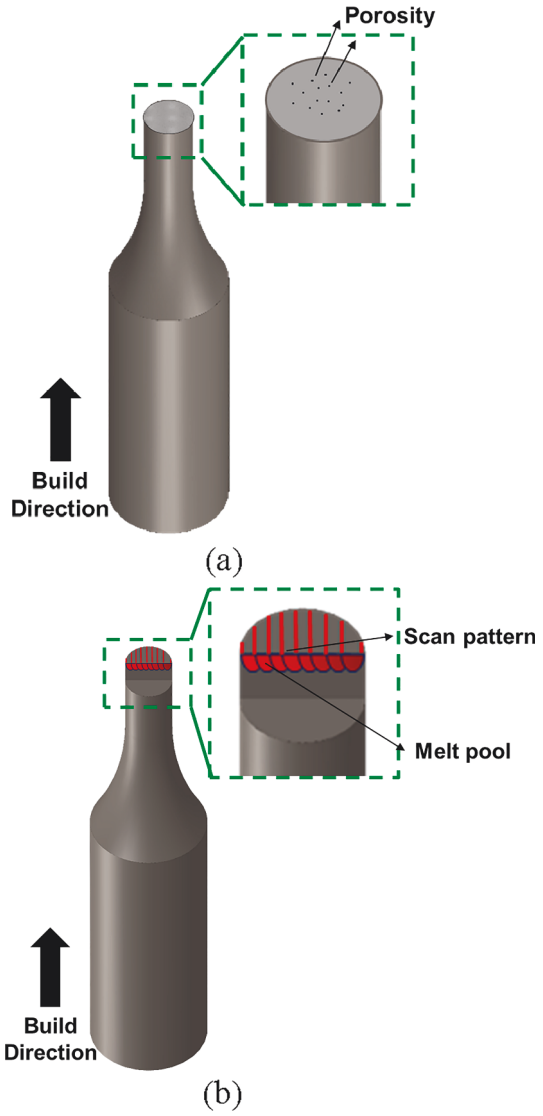

Fig. 3. Schematic illustration of (a) transverse plane (i.e. perpendicular to the build direction) for porosity analysis and (b) longitudinal plane (i.e. parallel to the building direction and perpendicular to the scan direction) for melt pool evaluation at the representative gage sections. The same approach was used for all geometries.

Table 2
Melt pool sizes including melt pool depth, d_p, melt pool overlap depth, d_o, along with their ratio to layer thickness, t_L, obtained for DB as well as SB and LB specimens, fabricated with different process parameters.

Specimen	d_p (μm)	d_p/t_L	d_o (μm)	d_o/t_L
Small Block				
SB Default	156	~3.9	80	~2.0
Dog-bone				
DB7.5$^-$	145	~3.6	75	~1.8
DB10$^-$	152	~3.8	83	~2.1
DB15$^-$	154	~3.9	90	~2.3
Large Block				
LB7.5$^+$	160	~4.0	78	~1.9
LB10$^+$	158	~3.9	79	~2.0
LB20$^+$	152	~3.8	70	~1.7

different geometries were fabricated using default process parameters, the variation seen in the defect distribution was assumed to be resulting from the variation in thermal history, which consequently, affected the fatigue behavior [5].

In the current study, the same three geometries (i.e. oversized dog-bone, small block, and large block) were fabricated; however, the oversized dog-bone and large block parts were fabricated by altering the scanning speed, while the manufacturer recommended process parameters were used for the fabrication of small block parts. The main idea behind varying the process parameters was to maintain a similar thermal history in all three geometries. In the previous study, the higher amount of porosity in dog-bone parts was attributed to the higher solidification rate, while the lower amount of porosity in large block parts was related to the lower solidification rate [5]. Therefore, in the present study, the value of scanning speed was decreased by 7.5%, 10%, and 15% of the default value in oversized dog-bone parts, and increased by 7.5%, 10%, and 20% of the default value in large block parts during LB-PBF fabrication, as listed in Table 1.

All parts were fabricated in the vertical direction following the build layout shown in Fig. 1 in an EOS M290, an LB-PBF machine, with nitrogen as the shielding gas. As can be seen from the figure, all of the parts were fabricated together and scattered throughout the build plate to minimize the effects of time interval (~62 sec) [8,37] and the location dependency [38], respectively. In addition, for the combination of each geometry type and process parameter set, some parts were fabricated up to the middle of the gage section (half-built parts). As the laser beam rotates by 67° every layer and the subsequent layer can also influence the previously solidified layers, the half-built parts were used to determine the exact direction of the laser scanning lines on the top layer for an accurate melt pool analysis [5,39].

Once the parts were removed from the build plate, fatigue specimens with uniform gage section were machined from oversized dog-bone as well as square blocks (i.e. small and large blocks), as schematically shown in Fig. 2(a). For simplicity, specimens machined from the oversized dog-bone, small block, and large block parts will be hereon referred to as DB, SB, and LB specimens, respectively. The number following the specimen name will represent the % value of scanning speed altered from the default value for the fabrication of that particular specimen. Moreover, the negative symbol will represent the decrease, and the positive symbol will represent the increase in the value of scanning speed. For instance, LB7.5$^+$ will represent an LB specimen fabricated by increasing the scanning speed by 7.5% of the default value. The final specimen geometry was designed based on ASTM E606 [40] (with the exception of the gage diameter) and the dimensions shown in Fig. 2(b). Due to the fact that all specimens in this study were machined deep enough, there should not be any effects of contour process parameters on the mechanical testing results.

To diminish the influence of microstructure and solely focus on the effect of defects on the fatigue behavior, all specimens were subjected to CA-H1025 heat treatment using a batch furnace in an argon environment after the machining process. The specimens were first solution treated at 1922 °F for half an hour and then air cooled to the room temperature, which is known as condition A. Following the solution treatment, the specimens were aged at 1025 °F for four hours, followed again by air cooling. Since this heat treatment has been reported to homogenize the microstructure of LB-PBF 17-4 PH SS [5,41], all specimens should have had similar constituent phases, although fabricated using different process parameters. It is also worth mentioning that as the specimens were not subjected to the hot isostatic pressing (HIPing), the applied heat treatment is not expected to affect the size and distribution of the volumetric defects [41].

2.2. Mechanical testing

Uniaxial, fully-reversed strain-controlled fatigue tests ($R_\varepsilon = -1$) were conducted only at the strain amplitude of 0.003 mm/mm at which

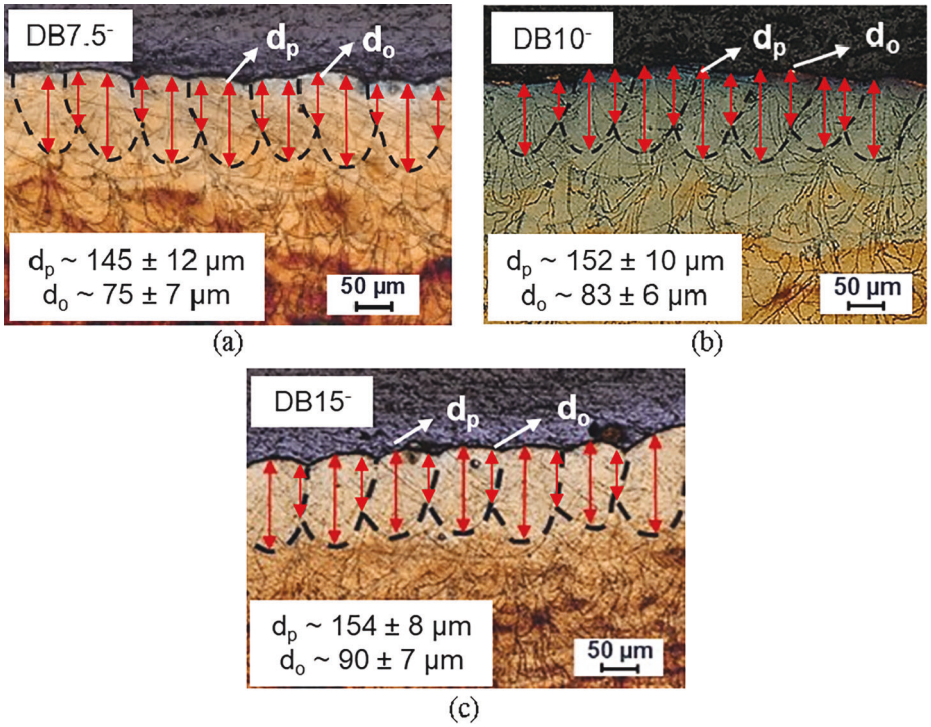

Fig. 4. Melt pool micrographs for DB parts along with the average values of melt pool depth, d_p, and overlap depth, d_o, fabricated with (a) 7.5% (b) 10% and (c) 15% lower value of the default scanning speed.

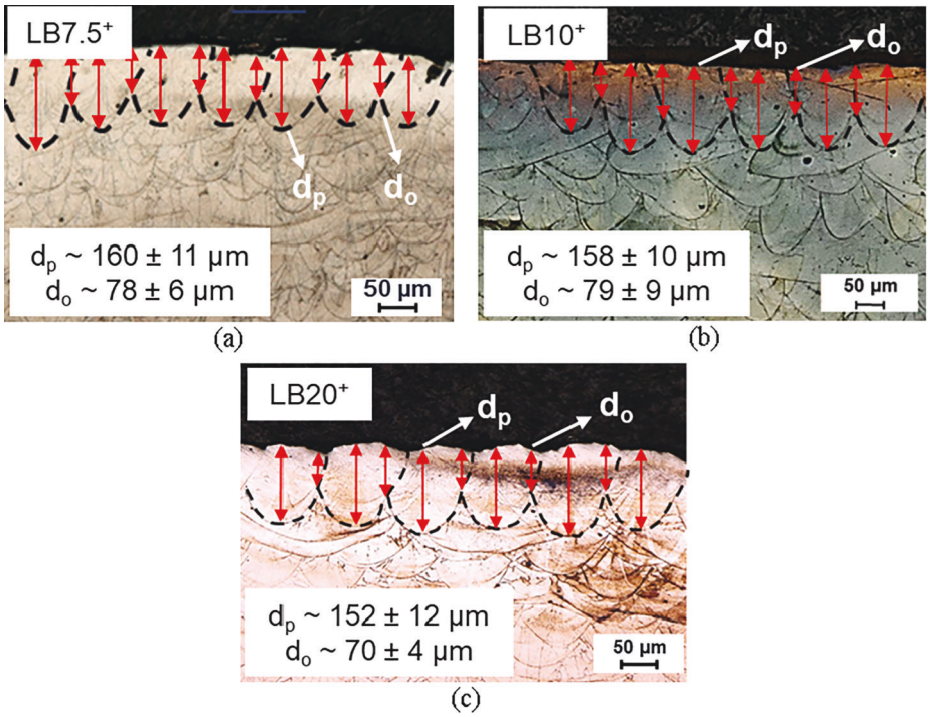

Fig. 5. Melt pool micrographs for LB parts along with the average values of melt pool depth, d_p, and overlap depth, d_o, fabricated with (a) 7.5% (b) 10% and (c) 20% higher value of the default scanning speed.

the effect of part geometry was seen to be significant in the first part of this study [5]. All of the fatigue tests were performed using an MTS Landmark, a closed-loop servo-hydraulic test frame with 100 kN load cells, and the localized deformation on the gage section of the specimen was measured using an MTS extensometer with a gage length of 12.7 mm. From the recent study, the deformation behavior of 17-4 PH SS at 0.003 mm/mm strain amplitude was observed to be fully elastic [41]. Hence, to protect the extensometer, strain-controlled tests were first conducted to obtain stable force values; the tests were then switched to the force-controlled mode and continued until fracture.

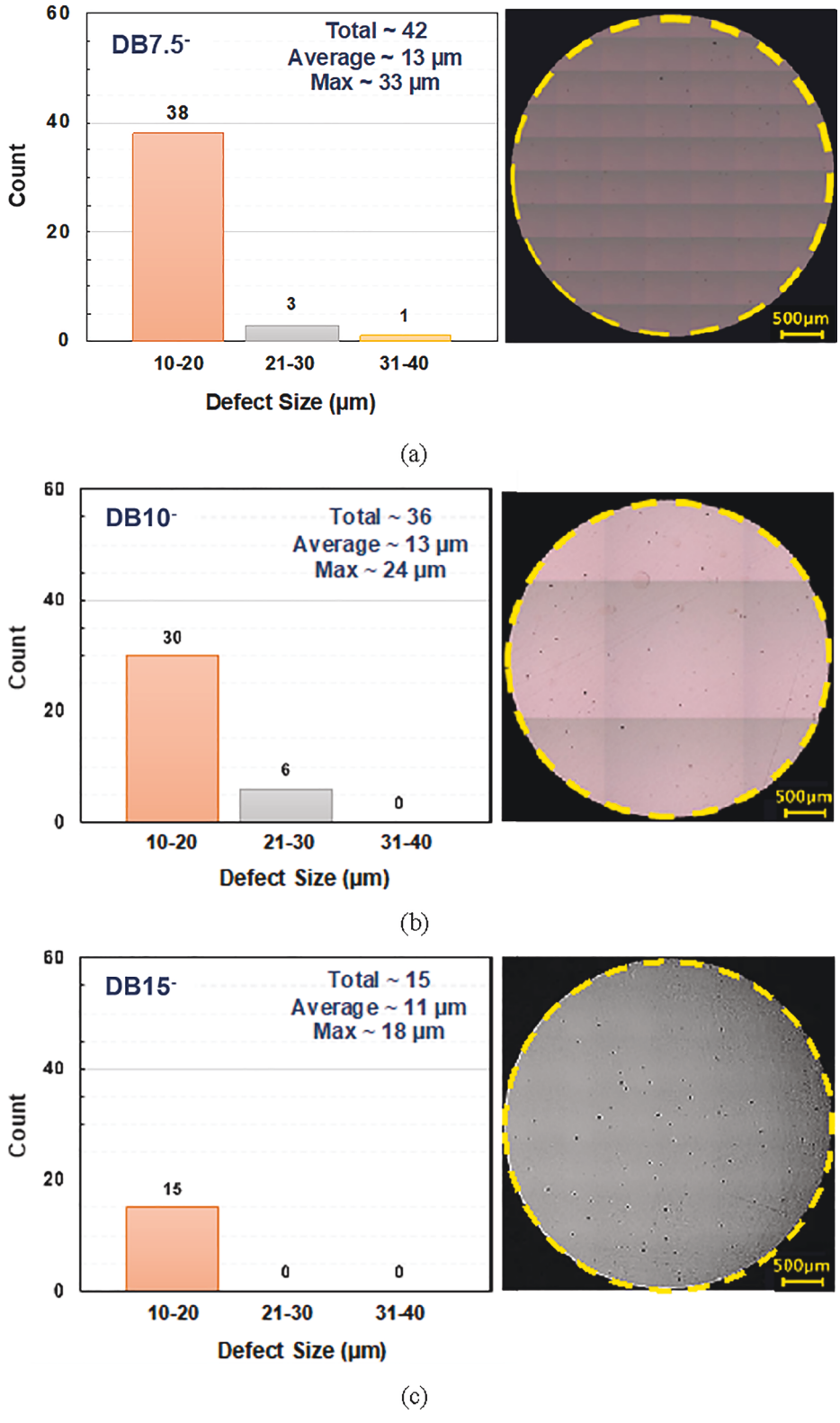

Fig. 6. Pore size distribution in the DB specimens fabricated with (a) 7.5%, (b) 10%, and (c) 15% lower value of the default scanning speed.

2.3. Microstructure and fractography analysis

Two different types of microstructural analyses were conducted in the current study to investigate the effect of process parameters, part geometry, and thermal history on the porosity distribution and the melt pool characteristics of LB-PBF 17-4 PH SS. For both microstructural analyses, non-heat treated half-built parts were first cut in the desired direction (i.e. transverse or longitudinal), and cold mounted in an epoxy resin solution. Mounted samples were then ground using different grit sandpapers followed by a polishing step using colloidal silica suspension to obtain a mirror-like surface finish. In the case of SB and LB samples, special care was taken to ensure that the porosity data as well as melt pool measurements were obtained from the locations representing the gage section of the fatigue specimens after machining.

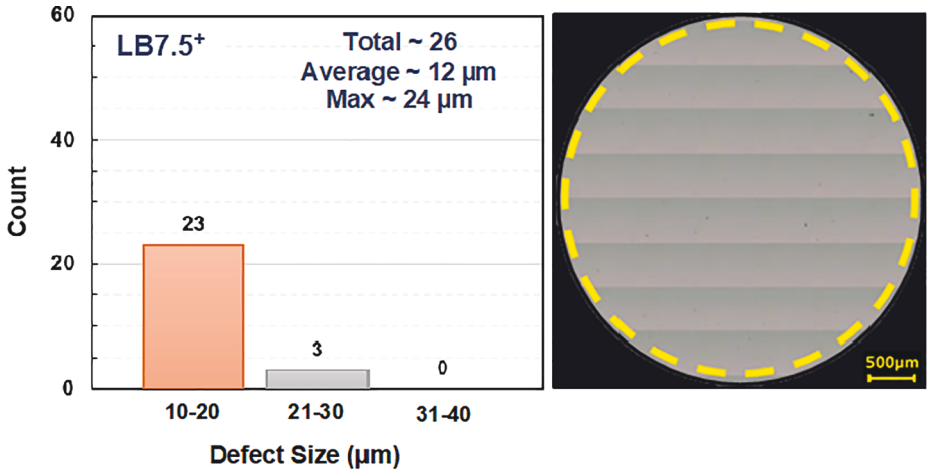

(a)

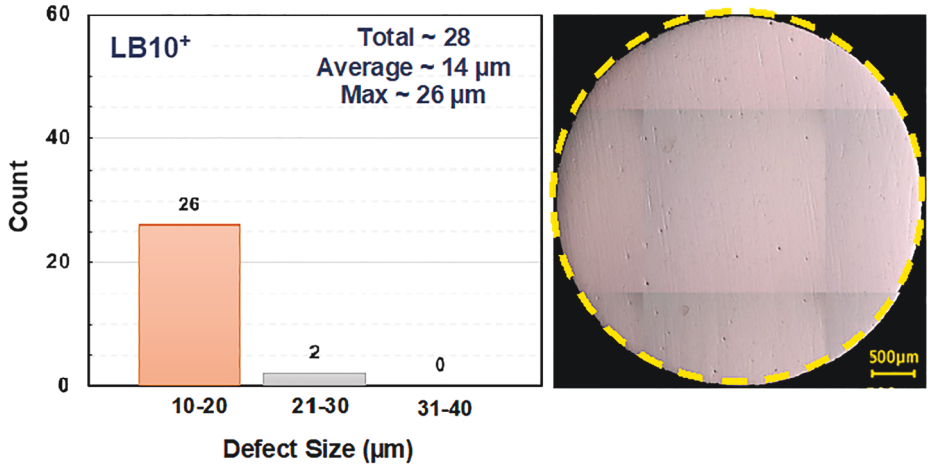

(b)

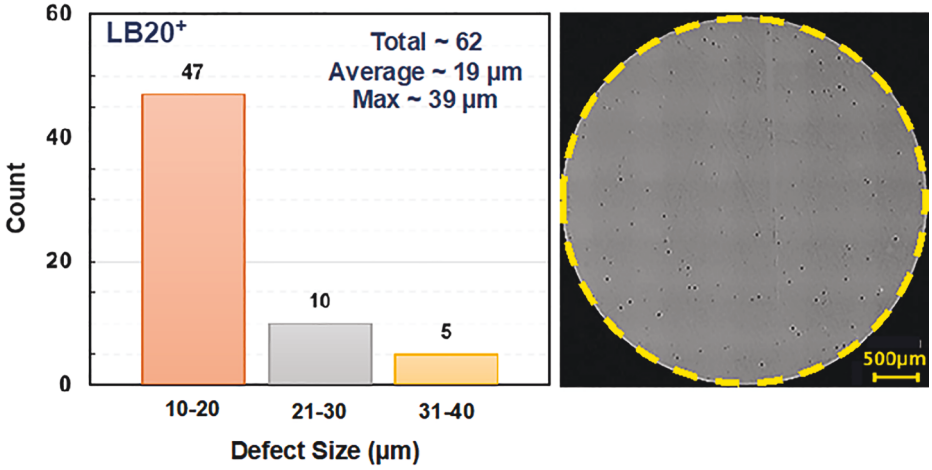

(c)

Fig. 7. Pore size distribution in the LB specimens fabricated by (a) 7.5%, (b) 10%, and (c) 20% higher value of the default scanning speed.

For the 2D porosity analysis, samples were cut in the transverse direction (perpendicular to the build direction) of parts, as shown in Fig. 3 (a), and polished to a mirror-like finish. Porosity data was obtained using a digital microscope and analyzed using the image processing software associated with the microscope. After acquiring porosity data, the polishing steps and porosity analysis were repeated multiple times (at least four) in different gage cross-sectional areas to achieve a general idea for the size distribution of pores throughout the gage section of the specimen. In addition, the defects smaller than 10 µm were not considered in porosity evaluation.

As the melt pool depths are typically greater than the layer thickness, melt pools of the new layer can influence the melt pools generated in the previously solidified layers. As a result, melt pool analyses were conducted on the top layer of the half-built parts. To accurately determine

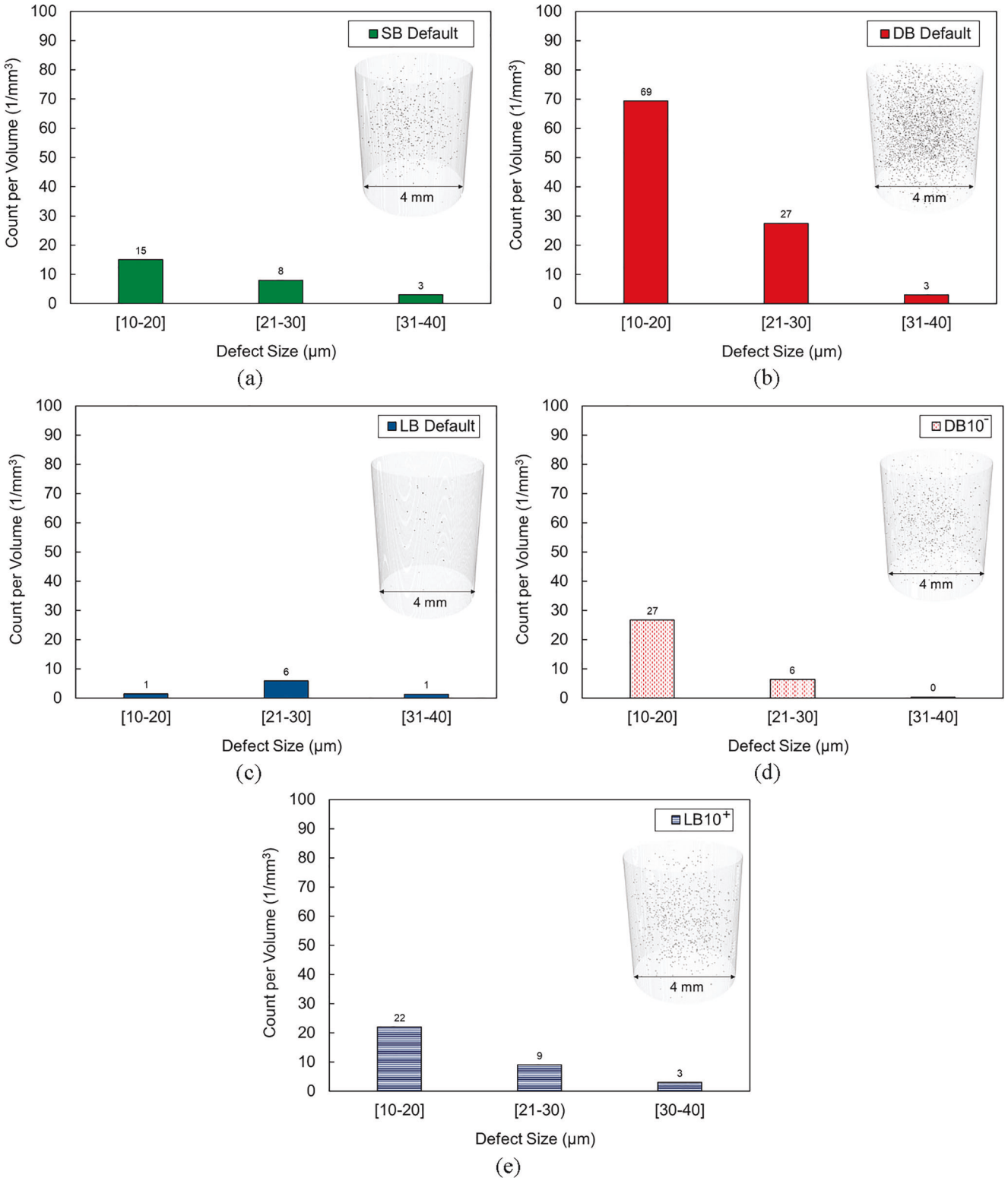

Fig. 8. Bar plots showing the range of defect obtained using 3D image analysis along with X-ray CT images showing the distribution of defects in the (a) SB, (b) DB, and (c) LB with default scanning speed, as well as (d) DB specimen with 10% reduction in scanning speed ($DB10^{-}$) and (d) LB with 10% increase in scanning speed ($LB10^{+}$).

the melt pool characteristics including the depths and overlap depths between two successive tracks, samples were cut longitudinally, perpendicular to the scan direction, as shown in Fig. 3(b). Cut samples were then mounted and polished using a similar procedure described previously. Mounted and polished samples were etched using Beraha's tint etchant to reveal the synergistic effects of process parameters and part geometry on the melt pool characteristics of LB-PBF 17-4 PH SS.

Finally, fracture surfaces of the failed specimens were also evaluated to determine the factors responsible for crack initiation and failure mechanisms in LB-PBF 17-4 PH SS specimens. For the fractography

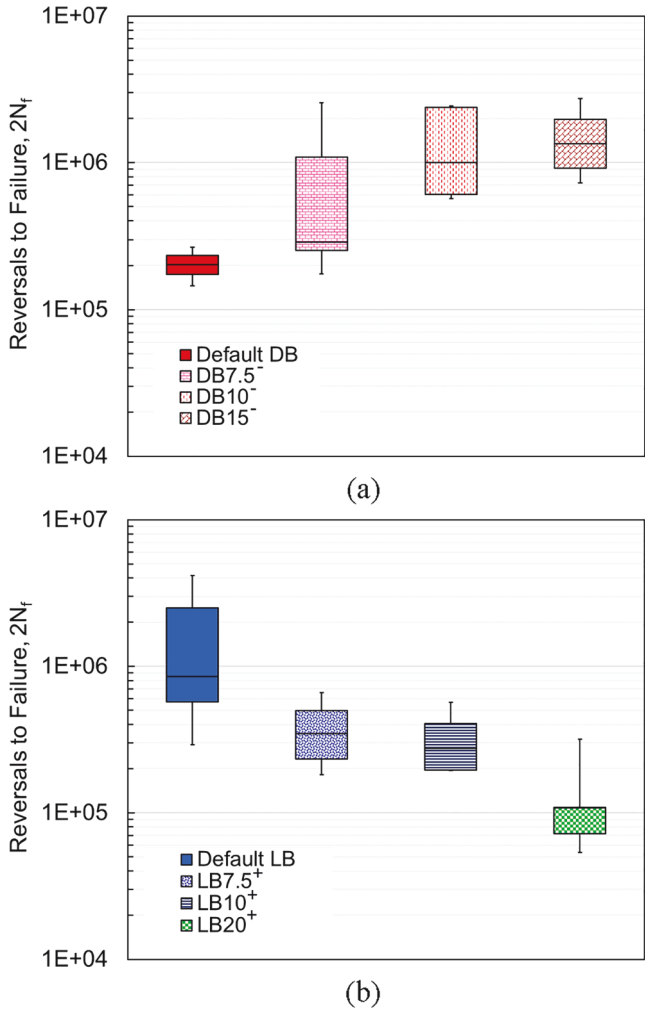

Fig. 9. Box plots illustrating the range of fatigue lives obtained for (a) DB specimens fabricated using default process parameters, as well as 7.5% (DB7.5$^-$), 10% (DB10$^-$), and 15% (DB15$^-$) reduction in scanning speed, and (b) LB specimens fabricated by default process parameters, as well as 7.5% (LB7.5$^+$), 10% (LB10$^+$), and 20% (LB20$^+$) increase in scanning speed. All specimens were tested at ε_a = 0.003 mm/mm. Fatigue data for DB and LB specimens manufactured using default process parameters were adapted from Ref. [5].

analysis, the fracture surfaces were first removed from the failed specimen, sonicated in an ethyl alcohol bath to remove any impurities such as dust particles, and then mounted in an aluminum stub. Special care was taken not to touch the fracture surface during the removal, cleaning, and mounting process. All microstructural (i.e. porosity and melt pool), as well as fractography analyses in this study, were conducted using a Keyence VHX-6000 digital microscope.

To obtain a 3D accurate representation of the porosity distribution, X-ray computed tomography (CT) was also conducted using a Zeiss Xradia 620 Versa with a maximum voltage of 160 kV and power of 25 W. In the case of 17-4 PH SS, a voltage of 140 kV and 21 W power was used along with an exposure time of 2 s and 0.4× magnification. The voxel size was determined to be ~5 μm. Post scanning image reconstruction was conducted using the Dragonfly software and the 3D porosity analysis was conducted using ImageJ and defects smaller than 10 μm were excluded from the analysis because of the lower confidence in measuring smaller pores. In addition, for the 3D porosity analysis, the characteristics including size and number of defects were normalized by the volume of the scanned gage section. On the other hand, in the 2D porosity analysis, defect size and numbers were determined by averaging the values obtained from a single layer at four different sections. Therefore, the results obtained from 2D and 3D porosity analysis may not be identical but both results should provide similar information on the general trend of defect distribution resulting from variations in the geometry and scanning speed.

3. Experimental results

3.1. Microstructural analysis

In an effort to maintain a similar thermal history among different geometries in this study, DB and LB parts were fabricated using different increments of scanning speeds; decreasing for DB and increasing for LB. As the thermal history is expected to affect the melt pool morphology, the melt pool depth, d_p, and the overlap depth between the consecutive melt pools, d_o, were measured for parts fabricated using various scanning speeds. These melt pool morphologies were determined based on the procedure proposed by NASA Marshall Space Flight Center (MSFC) [39] and are presented in Table 2 along with the ratio of melt pool depth and melt pool overlap depth to layer thickness, t_L.

Melt pools for DB7.5$^-$, DB10$^-$, and DB15$^-$ parts are shown in Fig. 4(a), 4(b), and 4(c), respectively. In addition, the average values of melt pool depths and the overlap depths determined for each part are also listed. By decreasing the scanning speed, the average melt pool depth, d_p, was observed to increase from the DB part fabricated with the default process parameters (~142 μm [5]) to ~145 μm for DB7.5$^-$, ~152 μm for DB10$^-$ and ~154 μm for DB15$^-$ parts. Along with the average values of melt pool depth, the average value of melt pool overlap depth, d_o, was also seen to vary with the employed process parameter. The melt pool overlap depth also increased by decreasing the scanning speed from ~72 μm in parts fabricated using default process parameters to ~75 μm in DB7.5$^-$, ~83 μm in DB10$^-$ and ~90 μm in DB15$^-$ parts. It is also worth mentioning that the melt pool overlap depth was seen to be more sensitive to the employed process parameters as compared to the melt pool depth. For instance, the melt pool depths were almost similar for DB10$^-$ and DB15$^-$ parts, while the melt pool overlap depths were considerably different.

Similar to the DB parts, the melt pool morphology for LB7.5$^+$, LB10$^+$, and LB15$^+$ parts are also determined and presented, respectively, in Fig. 5(a), 5(b), and 5(c). By increasing the scanning speed, the value of d_p was seen to decrease from ~162 μm in the LB parts fabricated with default process parameters [5], to ~160 μm in LB7.5$^+$, ~158 μm in LB10$^+$, and ~152 μm in LB20$^+$ parts. Moreover, with the increase in the scanning speed, the value of d_o was also seen to decrease from 81 μm for the LB part fabricated using the default process parameters [5] to ~78 μm for LB7.5$^+$, ~79 μm for LB10$^+$, and ~70 μm for LB20$^+$ parts.

The variation in the thermal history represented by the melt pool morphology is expected to also affect the porosity distribution. Accordingly, porosity analysis was conducted at four different locations at the gage section for both DB and LB specimens fabricated with varying scanning speeds in order to gain a better understanding of defect distribution through the gage section of the specimens. Bar charts showing the number of defects for a particular range along with the total number, average value, and the maximum defect size are presented in Fig. 6(a), 6(b), and 6(c), respectively, for DB7.5$^-$, DB10$^-$, and DB15$^-$ specimens. In addition, the dashed lines in the accompanied micrographs represent the area from where the porosity analysis was conducted (i.e. representing 4 mm diameter gage section), and only defects greater than 10 μm were considered for the analysis.

The total number of pores, as well as the average and maximum defect sizes, were seen to decrease by reducing the scanning speed by 7.5–15% of the default value. These bar charts reveal that the larger pores in the range of 31–40 μm were only observed in the DB7.5$^-$ part, while they were absent in DB10$^-$ and DB15$^-$ parts. In addition, defects between the range of 21–30 μm were absent in the DB15$^-$ specimen. In general, the porosity was seen to have a decreasing trend by decreasing

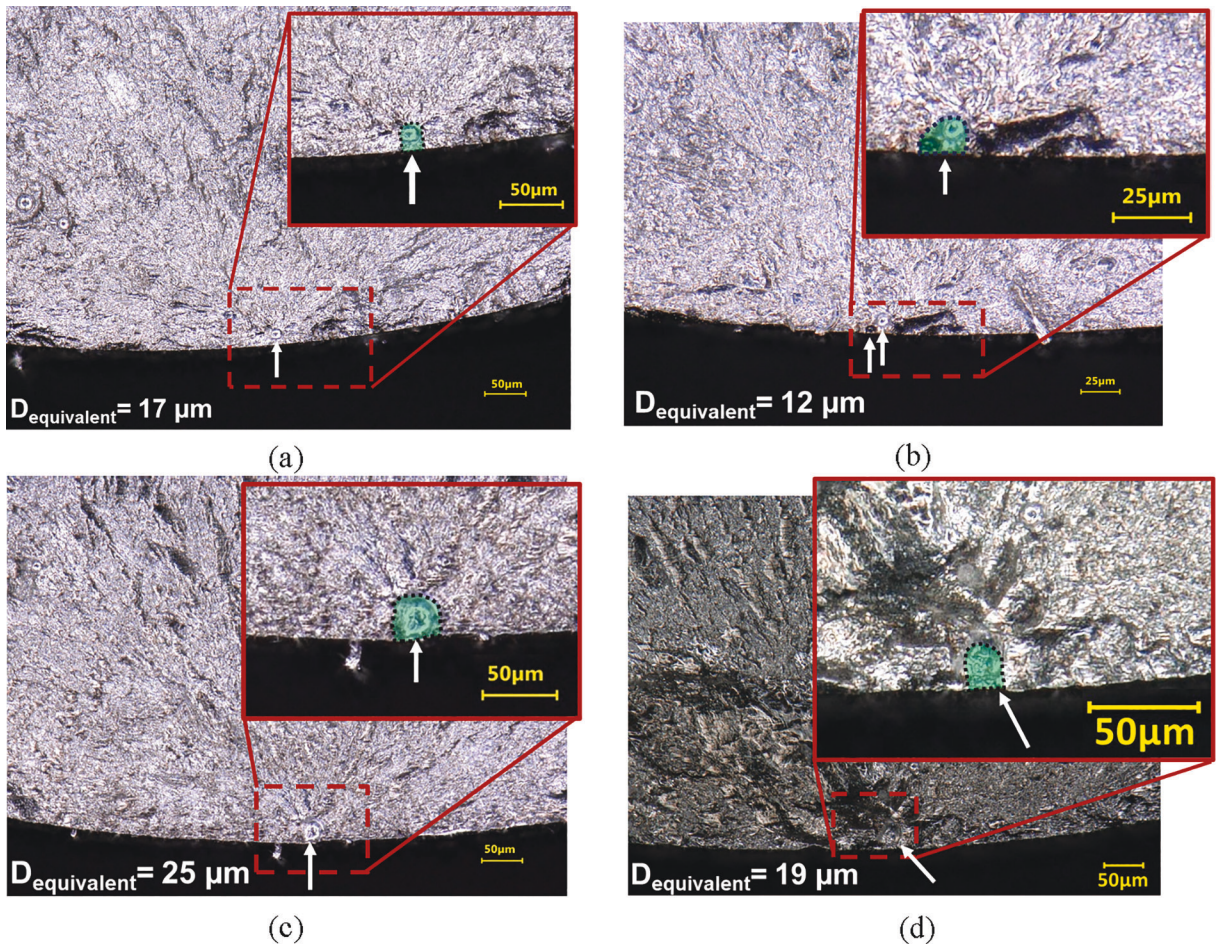

Fig. 10. Fracture surfaces of LB-PBF CA-H1025 17-4 PH SS for (a) a $DB10^-$ specimen with a fatigue life of 568,750 reversals, (b) a $DB15^-$ specimen with a fatigue life of 1,716,236 reversals, (c) an $LB10^+$ specimen with a fatigue life of 196,450 reversals, and (d) an $LB10^+$ specimen with a fatigue life of 569,088 reversals. All specimens were tested at $\varepsilon_a = 0.003$ mm/mm.

the scanning speed from the default value up to 15% that has been investigated in this study.

In an attempt to increase the solidification rate in the LB specimen and to increase the porosity to the level of the SB specimens with default process parameters, the scanning speed was increased by 7.5%, 10%, and 20% of the default value. Similar porosity analyses to the ones conducted for the DB specimens were done for the LB specimens to determine the total number, average and maximum size of defects, and the results are shown in Fig. 7. As expected, increasing the scanning speed resulted in an increase in porosity in LB specimens. The total number of defects was seen to increase from 23 to 62 for LB specimen fabricated using the default process parameters [5] and $LB20^+$ in Fig. 7, respectively. Additionally, the total number of defects and average and maximum defect sizes were somewhat similar in $LB7.5^+$ and $LB10^+$ specimens, which also had similar melt pool morphologies, suggesting that both specimens may have experienced similar thermal histories. On the other hand, a greater number of large defects in the range of 21–30 μm as well as 31–40 μm were present in the $LB20^+$ specimens, when compared to $LB7.5^+$ and $LB10^+$ specimens.

In the 2D porosity analysis conducted in Ref. [5], for SB parts fabricated using default process parameters, the total number of defects, and average and maximum defect sizes were observed to be respectively, 31, 11 μm, and 23 μm. In the current study, for the DB and LB parts fabricated using altered scanning speed, the closest defect distribution was observed for $DB10^-$ parts with a total defect of 36, an average pore size of 13 μm, and the maximum pore size of 24 μm. In the case of LB parts, porosity distribution of $LB10^+$ with total defects of 28, an average pore size of 14 μm, and the maximum pore size of 26 μm were found to be the closest to the SB parts with default process parameter. Therefore, based on the 2D porosity analysis, SB with default process parameter, $DB10^-$, and $LB10^+$ parts are assumed to exhibit similar fatigue behaviors.

To better understand the distribution of defects, 3D porosity analysis was also conducted using an X-ray CT on selected specimens, which exhibited similar defect distribution obtained by the 2D porosity analysis. Bar plots showing the range of defects obtained from the 3D defect analysis along with the reconstructed X-ray CT images of the gage section of SB, DB, and LB specimens with default process parameters as well as $DB10^-$ and $LB10^+$ specimens are presented in Fig. 8(a)–8(e), respectively. Based on the X-ray CT analysis, the defects in the DB specimens were observed to decrease by reducing the scanning speed, while the defects in the LB specimens were increased by increasing the scanning speed.

Both X-ray CT images, and the pore size distributions obtained from the 3D as well as 2D defect analyses, reveal that the distribution of defects between SB with default process parameter, $DB10^-$, and $LB10^+$ specimens are somewhat comparable. However, the $DB10^-$ has fewer larger defects, which is expected to result in some improvement in the fatigue life of these specimens. It is also important to mention that the results for 2D porosity analysis were obtained by averaging the defects observed by sectioning the gage at four different locations. However, the results obtained from the 3D porosity analysis were normalized by dividing the number of defects by the volume of the scanned section of the specimen's gage. Therefore, the results obtained from 2D and 3D analyses are not comparable; nonetheless, the range of defects, as well as

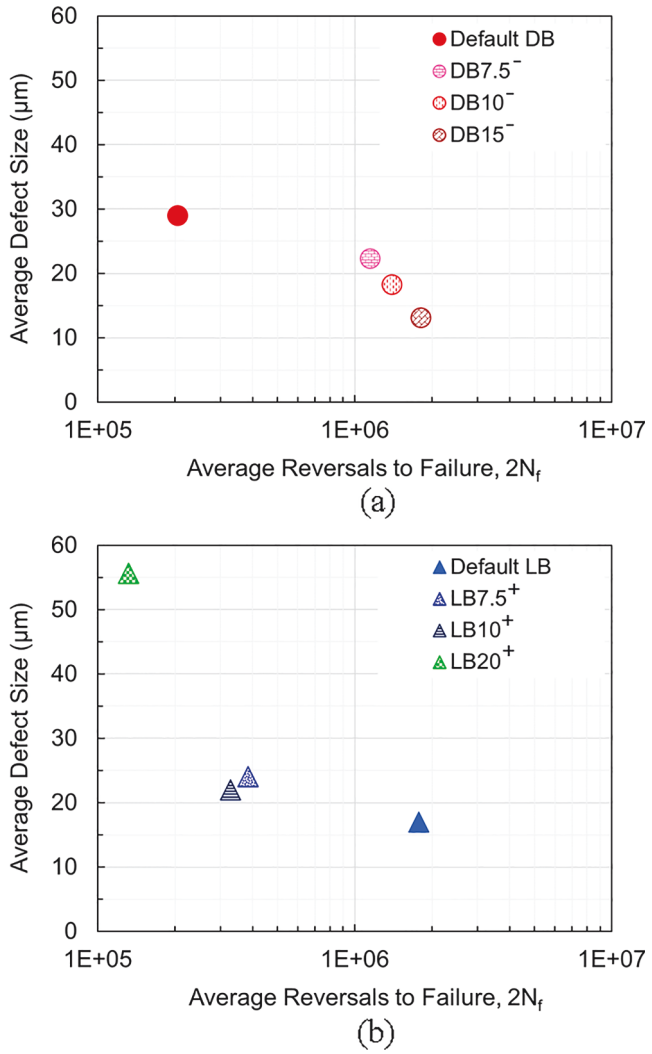

Fig. 11. Average fatigue lives versus average defect size obtained by Murakami's approach [42] for (a) DB specimens fabricated using default process parameters, as well as 7.5% (DB7.5$^-$), 10% (DB10$^-$), and 15% (DB15$^-$) reduction in scanning speed, and (b) LB specimens fabricated using default process parameters, as well as 7.5% (LB7.5$^+$), 10% (LB10$^+$), and 20% (LB20$^+$) increase in scanning speed. All specimens were tested at $\varepsilon_a = 0.003$ mm/mm.

the trend of the increasing and decreasing in defects' size and number, are similar in both 2D and 3D assessments.

3.2. Fatigue results and fractography analysis

Altering the process parameters for the fabrication of parts with different geometries was seen to affect the thermal history (indicated by the change in melt pool characteristics) and the level of the volumetric defects in the fabricated material. In addition, as these pores can directly affect the fatigue lives of AM parts, the employed process parameters can eventually affect the fatigue behavior of LB-PBF 17-4 PH SS specimens. Fatigue lives obtained for DB and LB specimens fabricated using altered scanning speeds along with the ones fabricated using default process parameters [5] are shown in Fig. 9, as box plots presenting the first-, second- (i.e. median), and third-quartile fatigue lives along with the whisker plots showing the maximum and minimum fatigue lives. As can be seen from the chart, the median fatigue life increased by decreasing the scanning speed for DB specimens, while the fatigue life decreased by increasing the scanning speed for the LB specimens. Therefore, based on the melt pool characterization and porosity measurements, controlling the input energy density, by altering for example the scanning speed to vary the thermal history experienced by the part during the AM process, can eventually affect the fatigue behavior.

The fractography analysis was performed to determine the factors responsible for crack initiation and failure in LB-PBF 17-4 PH SS fabricated using different scanning speeds. The fracture surfaces of selected specimens are shown in Fig. 10. The defect sizes, represented by the equivalent diameter, $D_{equivalent}$, were evaluated using Murakami's approach and portrayed with green overlaid areas in this figure. Based on this approach, for the cracks initiating from multiple defects that are located at a distance smaller than the diameter of the smallest defect, the defect size is calculated as the square root of the semi-circle enveloping all these adjacent defects, which is illustrated in Fig. 10(b). Moreover, when the defect size is larger than its distance to the surface, the defect is considered as a surface defect. In this condition, the defect size is considered as the square root of the semi-circular envelope from the surface, hence, incorporating both size and location of the defect. Additional criteria for determining the defect size based on Murakami's approach are given in Ref. [42].

The fracture surfaces revealed that the fatigue life was dictated by the size of a single and in some cases a cluster of multiple entrapped-gas pores located in the proximity of each other in most specimens. In addition, all crack initiating defects were seen to be located either at the surface or close to the surface of the specimen. For instance, a fatigue crack was observed to initiate from a 17 μm entrapped-gas pore in DB10$^-$ specimen with the fatigue life of 568,750 reversals, shown in Fig. 10(a), while a smaller 12 μm entrapped-gas pore, shown in Fig. 10(b), was found responsible for the crack initiation in DB15$^-$ specimen with a longer fatigue life of 1,716,236 reversals. A similar observation was also made for LB specimens; the LB10$^+$ specimen (see Fig. 10(c)), which lasted for 196,450 reversals failed due to a 25 μm entrapped-gas pore, while another LB10$^+$ specimen with a longer fatigue life of 569,088 reversals (see Fig. 10(d)) failed due to a smaller entrapped-gas pore of 19 μm.

To further relate the results obtained from the microstructural investigation (melt pool and porosity distribution) and the fatigue tests, fractography analysis for each of the failed specimens was conducted to determine the type and size of defects responsible for initiating the fatigue crack growing to cause the final fracture. The average defect size observed from the fractography analysis versus the average fatigue lives is presented in Fig. 11(a) and 11(b), respectively, for DB and LB specimens fabricated with different scanning speeds. The defect size responsible for the fatigue failure seems to move to the desired direction as increasing the scanning speed for LB specimens resulted in larger defects and shorter fatigue lives. On the other hand, for DB specimens, decreasing scanning speed resulted in smaller defects, and subsequently, longer fatigue lives. All defect sizes presented in Fig. 11 were also evaluated using Murakami's approach.

4. Discussion on fatigue results

Fatigue life data obtained for DB and LB specimens fabricated using different process parameters are shown in Fig. 12, which also includes the line charts representing the range of fatigue lives along with the data points obtained for DB, SB, and LB specimens fabricated using default process parameters in Ref. [5]. For the parts with different geometry fabricated using identical default process parameters, the lowest fatigue lives were seen for DB followed by SB, and the highest fatigue resistance was exhibited by LB specimens [5]. Hence, the objective of this study was to alter process parameters to obtain similar fatigue lives for DB and LB specimens with the ones for SB specimens fabricated by default process parameters (i.e. represented by the green horizontal dashed lines in Fig. 12). Among all the conditions investigated, DB10$^-$ and LB10$^+$ specimens appear to have the most similarities to the fatigue lives of SB specimens manufactured via default process parameters. Although the range of fatigue lives was not identical, they were similar enough considering the typical scatter observed in fatigue data. Therefore, it is

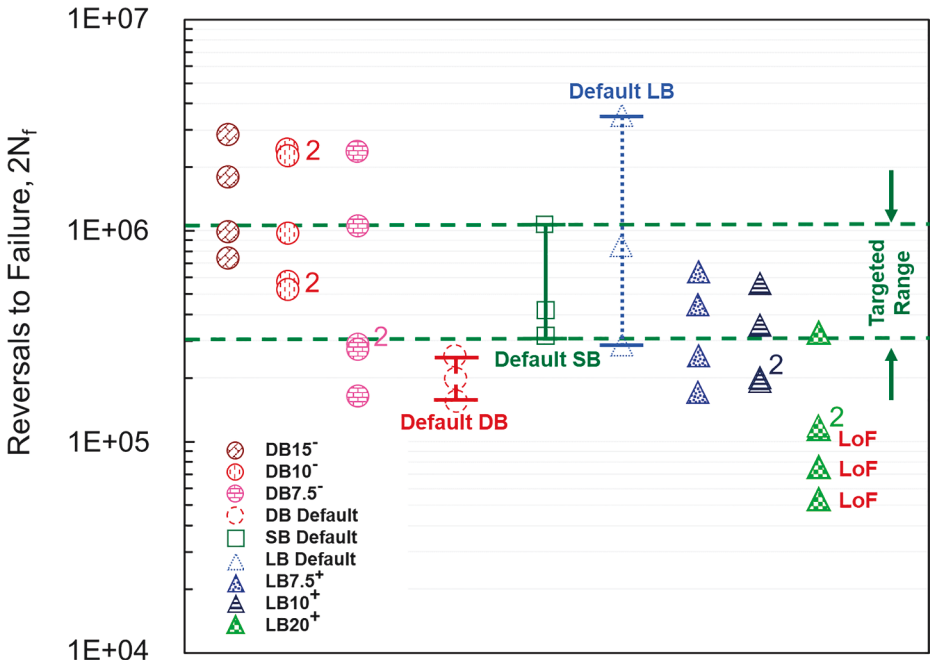

Fig. 12. Fatigue lives obtained for LB-PBF 17-4 PH SS DB specimens fabricated with 7.5% (DB7.5$^-$), 10% (DB10$^-$), and 15% (DB15$^-$) reduction in scanning speed, and LB specimens fabricated with 7.5% (LB7.5$^+$), 10% (LB10$^+$), and 20% (LB20$^+$) increase in scanning speed. All specimens were tested at ε_a = 0.003 mm/mm. The hollow data points and the bars represent the range of fatigue lives obtained for DB, SB, and LB specimens manufactured by default process parameters [5]. The targeted fatigue life range is the range of fatigue lives for SB specimens with default process parameters represented by the green horizontal dashed lines. (For interpretation of the references to colour in this figure legend, the reader is referred to the web version of this article.)

concluded that the fatigue lives of DB and LB can shift to the desired direction by altering the value of a single process parameter, i.e. the scanning speed in this study. However, better results may be obtained by altering more than one process parameter, or by reducing the incremental changes in the process parameters.

The similarity observed in the fatigue lives between SB specimens with default process parameters and DB10$^-$ and LB10$^+$ specimens may be attributed to the similarity in the thermal histories experienced by these parts. As seen in Table 2, the melt pool depths and melt pool overlap depths were found to be ~152 μm and ~83 μm for DB10$^-$ part, ~156 μm, and ~80 μm for the SB part with default process parameter, and ~158 μm and ~79 μm for LB10$^+$ parts. This similarity in melt pool characteristics may indicate that all three specimens have experienced similar thermal histories during fabrication, resulting in the similarity between melt pool morphologies as well as defect size distributions in DB10$^-$, SB, and LB10$^+$ parts. In addition, from the fractography analysis conducted for parts fabricated with different process parameters, the average defect sizes were seen to be very comparable for DB10$^-$ (i.e. ~19 μm), SB with default process parameter (i.e. ~20 μm [5]), and LB10$^+$ (i.e. ~22 μm), as seen in Fig. 11.

As mentioned earlier, the thermal history experienced by the part during fabrication is primarily governed by the employed process and design parameters. The process parameters utilized are primarily responsible for the melting of the powder layer, which also influences the amount of input energy during fabrication. Moreover, the thermal history in the part can be affected by the design parameters such as the part geometry/size, number of parts on the build plate, time interval, and more. In the previous study, by using identical process parameters, the thermal history experienced during the fabrication process, represented by the melt pool morphology, was found to be affected by the part shape and size. Shallower melt pools in DB (i.e. the smaller part) and deeper melt pools in LB (i.e. larger part) were associated with the higher and lower solidification rates, respectively [5].

The scanning speed was lowered in this study for fabricating DB parts in an attempt to increase the input energy. Higher input energy densities can result in a lower solidification rate as the previously solidified layer upon which a new layer is fabricated is at a higher temperature [43,44]. This lower solidification rate can result in higher absorbed energy in the part due to longer exposure time, and consequently, larger melt pools [45]. This is also supported by the observation that melt pool depth and overlap depth increase with the decrease in scanning speed. In the case of LB parts, the scanning speed was enlarged to increase the solidification rate, which resulted in decreased melt pool depth and overlap depth.

Among specimens fabricated using different scanning speeds, the LB20$^+$ specimens particularly showed a significant reduction in the fatigue resistance (see Fig. 12), owing to the presence of large defects in the material (see Fig. 7(c) and Fig. 11(b)). Upon fractography analysis, the cracks in LB20$^+$ specimens were seen to initiate from LoF defects, illustrated by white arrows in Fig. 13(a) and 13(b) for specimens with fatigue lives of 53,470 and 71,834 reversals, respectively. Since LoF defects are larger and more irregular-shaped than entrapped-gas pores, their effect on the fatigue strength is often more detrimental. The presence of these LoF defects in LB20$^+$ specimens can explain their very short fatigue lives. Nevertheless, fatigue cracks were observed to initiate from the entrapped-gas pores in all other DB and LB specimens manufactured with adjusted process parameters.

The value of scanning speed (~906 mm/s) and the laser power of 220 W, employed for the fabrication of LB20$^+$ specimens resulted in melt pool depths with an average size of 152 μm, which was appreciably greater than the layer thickness (i.e. 40 μm). Therefore, observing LoF defects derived from insufficient bonding between subsequent layers for these specimens was unexpected. In other words, the employed laser power and scanning speed should have ensued a melt pool depth capable of penetrating through multiple layers, resulting in a proper metallurgical bonding and eliminating the probability of LoF formation. However, it is notable from Table 2 that the overlap depth and overlap depth to layer thickness ratio of LB20$^+$ are consistently smaller (i.e. $d_o \sim 70$ μm and $d_o/t_L \sim 1.7$) than other parts including the SB part with default process parameter, for which $d_o \sim 80$ μm and $d_o/t_L \sim 2.0$.

Some studies have shown that the insufficient overlap between two adjacent melt pools can result in LoF defects [20,39,46], which cannot be avoided only by ensuring deep enough melt pools. Interestingly, the current $d_o/t_L \sim 1.7$ of LB20$^+$ part indicates that the melt pool overlap depth is also larger than the layer thickness, and thus, there should have been an adequate fusion between the two adjacent tracks and subsequent layers [20]. However, any anomalies during the manufacturing process can result in this ratio getting closer to (or even less than) 1, and consequently, form LoF defects in some locations.

Melt pool micrographs of an LB part fabricated using default process

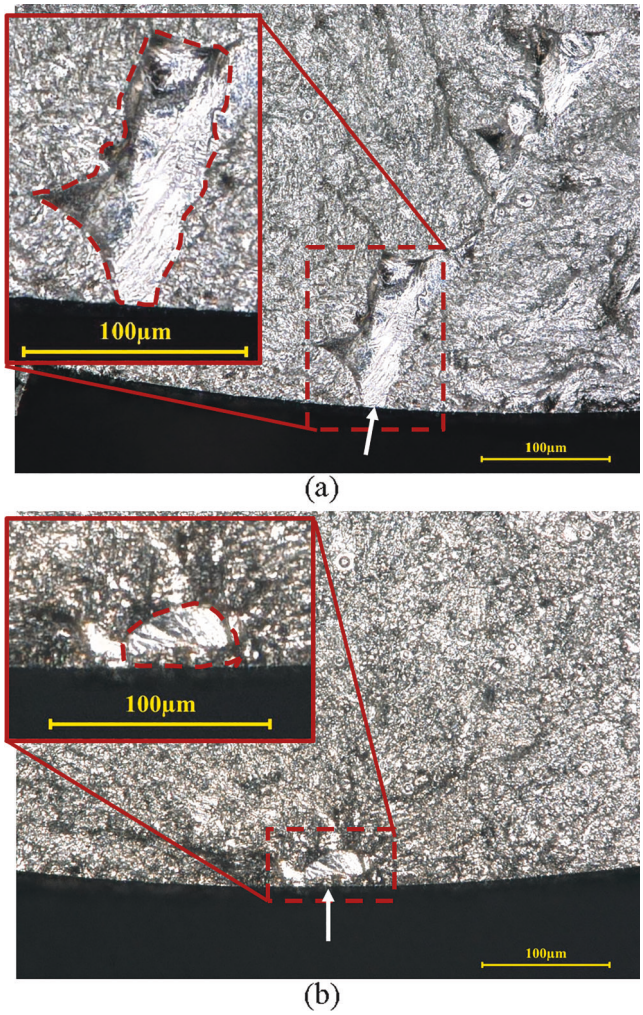

Fig. 13. Fracture surfaces of LB-PBF CA-H1025 17-4 PH SS LB20^{+} specimens tested at $\varepsilon_a = 0.003$ mm/mm with (a) 53,470 reversals and (b) 71,834 reversals to failure. Cracks were observed to initiate from LoF defects in these specimens.

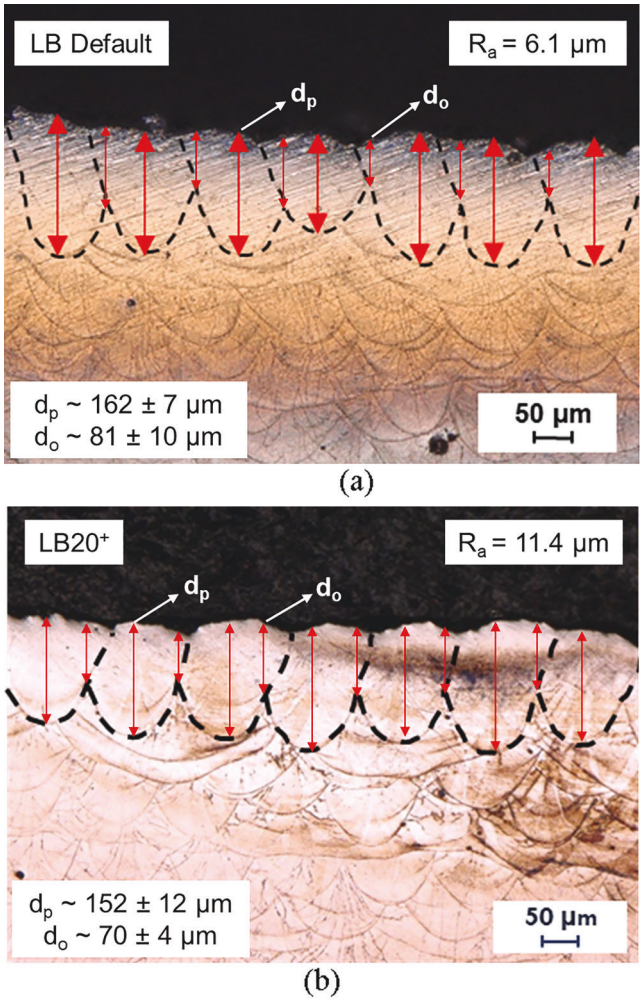

Fig. 14. Melt pool micrographs for LB parts manufactured by (a) default process parameters (LB Default) adapted from Ref. [5], and (b) 20% increase of the default scanning speed (LB20^{+}).

parameters and an LB20^{+} part are shown in Fig. 14(a) and 14(b), respectively. The top part of the melt pool in the LB20^{+} part was seen to be slightly rougher than the one in the LB part fabricated using the default process parameters. The surface roughness measurements conducted using the Keyence digital microscope along the direction perpendicular to the scanning tracks on the top of half-built parts revealed a higher surface roughness of $R_a \sim 11.4$ µm for LB20^{+} parts as compared to $R_a \sim 6.1$ µm for the LB parts with the default process parameter. This relatively higher surface roughness in LB20^{+} can adversely affect the powder spreadability, and consequently, the powder layer uniformity on top of the part during the subsequent recoating. Similarly, a higher surface roughness for the top layer associated with higher scanning speed is also reported in Ref. [47] for an LB-PBF aluminum alloy.

Considering the higher thermal conductivity of the solidified material compared to the powder, the melt pool may deflect towards the side with lower powder layer thickness because of directional heat flow within the melt pool [47]. This deflection of the melt pool may not affect the melt pool depth as much, but it can result in a smaller melt pool overlap depth and a reduction in d_o/t_L ratio to less than unity, leading to the formation of unexpected LoF defects. In addition, the probability for the occurrence of nonuniformity in the distribution of powder may be higher for the parts with the larger surface area. This is due to the higher possibility of scraping leading to powder layer disturbance during the powder distribution, which may be another reason that these LoF defects were generally seen in the LB20^{+} specimens. It is also important to note that these slit-shaped LoF defects are formed between the layers, which means that they can only exist in every 40 µm. As a result, the LoF defects will be easily missed when sectioning the gage in a few random locations for microscopy, as such, they were not observed from the 2D porosity analysis in Fig. 7(c).

Therefore, only considering the melt pool depths as a measure of reaching similarity in thermal histories between test specimens and the critical location of the part may not be adequate. The overlap depth between the consecutive melt pool tracks is also an important factor to consider for ensuring the properties measured from test specimens in the laboratory are representative of the part performance (i.e. property-performance relationships). It should be noted that many other factors such as powder specification and re-use, post-fabrication thermal and surface treatments, etc. can also affect the structure-property-performance relationships of AM materials and parts. However, based on observations and analyses performed in this study it appears that maintaining a similar thermal history between the laboratory specimens and the critical location of the part by altering process parameters is an important step towards establishing property-performance relationships and assuring that the mechanical properties obtained from the laboratory specimens can be representative of the part performance.

5. Conclusions

In the current study, the effects of altering scanning speed for parts with different geometries on the thermal history, defects formation and distribution, as well as fatigue behavior were investigated for 17-4 precipitation hardening (PH) stainless steel (SS) fabricated using laser beam powder bed fusion (LB-PBF) process. Melt pool characteristics such as the depth and overlap depth between melt pools of adjacent tracks were considered to represent the thermal history. The variations seen in the melt pool morphology were correlated to the defect size distribution, which could ultimately explain the fatigue lives obtained for specimens from parts with different geometries. Based on the experimental observations and analyses performed, the following conclusions can be drawn:

1. Melt pool analysis, conducted using optical microscopy, indicated that altering scanning speed could affect the thermal history experienced during AM, which was evident by the changes in melt pool depth and overlap depth between the melt pools from two adjacent tracks.
2. Increasing the amount of input energy density by decreasing the scanning speed during the fabrication of dog-bone parts decreased the solidification rate resulting in deeper melt pools, and consequently, fewer and smaller entrapped-gas pores. This reduction in porosity level helped to obtain longer fatigue lives for dog-bone specimens.
3. In the case of large block specimens, an increase in scanning speed resulted in shallower melt pools and their overlap depths, and consequently, larger and more defects, which decreased their fatigue lives.
4. Although the melt pool depth was seen to be almost three times of layer thickness, LoF defects were still formed in large block specimens fabricated using 20% increase from the default value of scanning speed. The presence of lack of fusion defects was attributed to smaller melt pool overlap depths in these specimens and the possibility of melt pool deflection, influenced by the potential process anomalies, resulting in the overlap depth to powder layer thickness ratio to occasionally become close or smaller than unity.
5. Similar thermal histories represented by similar melt pool depths and melt pool overlap depths were obtained in the dog-bone, small block, and large block specimens fabricated using 10% lower, default value, and 10% higher scanning speeds, respectively. In addition, the defect size distributions, and the resulting fatigue lives, were also observed to be similar among these specimens.

In summary, the results of this study indicate that any variations in the thermal history experienced by the part during fabrication can considerably affect the defect formation and the fatigue performance of the AM parts. It is also shown that the differences in the fatigue performance of parts with different geometries can be minimized by ensuring a similar structure (i.e. microstructure and porosity level) through maintaining a similar thermal history. This is an important factor for establishing property-performance relationships and generating reliable materials data for the design and qualification of AM products. It is worth mentioning that a reliable and experimentally validated thermal simulation, modeling, or monitoring package that can incorporate the effects of process and design parameters on the thermal history will be very helpful in designing AM parts based on the most representative materials data generated by specimen testing in the laboratory. Such a design tool can be used to ensure the gage section of the specimen and the critical location of the parts experience the same thermal history, and therefore, exhibit the same mechanical/fatigue strengths.

Declaration of Competing Interest

The authors declare that they have no known competing financial interests or personal relationships that could have appeared to influence the work reported in this paper.

Acknowledgments

This paper is based upon the work partially supported by the ASTM International Additive Manufacturing Center of Excellence (AM CoE) and the U.S. Naval Air Systems Command (NAVAIR). Rakish Shrestha is currently at the Sandia National Laboratories.

References

[1] Cunningham R, Narra SP, Ozturk T, Beuth J, Rollett AD. Evaluating the Effect of Processing Parameters on Porosity in Electron Beam Melted Ti-6Al-4V via Synchrotron X-ray Microtomography. JOM 2016;68:765–71. https://doi.org/10.1007/s11837-015-1802-0.
[2] Weingarten C, Buchbinder D, Pirch N, Meiners W, Wissenbach K, Poprawe R. Formation and reduction of hydrogen porosity during selective laser melting of AlSi10Mg. J Mater Process Technol 2015;221:112–20. https://doi.org/10.1016/j.jmatprotec.2015.02.013.
[3] Oliveira JP, LaLonde AD, Ma J. Processing parameters in laser powder bed fusion metal additive manufacturing. Mater Des 2020;193:1–12. https://doi.org/10.1016/j.matdes.2020.108762.
[4] Kruth JP, Levy G, Klocke F, Childs THC. Consolidation phenomena in laser and powder-bed based layered manufacturing. CIRP Ann - Manuf Technol 2007;56:730–59. https://doi.org/10.1016/j.cirp.2007.10.004.
[5] Shrestha R, Shamsaei N, Seifi M, Phan N. An investigation into specimen property to part performance relationships for laser beam powder bed fusion additive manufacturing. Addit Manuf 2019;29:100807. https://doi.org/10.1016/j.addma.2019.100807.
[6] Shrestha R, Simsiriwong J, Shamsaei N. Fatigue behavior of additive manufactured 316L stainless steel parts: Effects of layer orientation and surface roughness. Addit Manuf 2019;28:23–38. https://doi.org/10.1016/j.addma.2019.04.011.
[7] Cutolo A, Engelen B, Desmet W, Van Hooreweder B. Mechanical properties of diamond lattice Ti–6Al–4V structures produced by laser powder bed fusion: On the effect of the load direction. J Mech Behav Biomed Mater 2020. https://doi.org/10.1016/j.jmbbm.2020.103656.
[8] Yadollahi A, Shamsaei N, Thompson SM, Seely DW. Effects of process time interval and heat treatment on the mechanical and microstructural properties of direct laser deposited 316L stainless steel. Mater Sci Eng A 2015;644:171–83. https://doi.org/10.1016/j.msea.2015.07.056.
[9] Razavi SMJ, Van Hooreweder B, Berto F. Effect of build thickness and geometry on quasi-static and fatigue behavior of Ti-6Al-4V produced by Electron Beam Melting. Addit Manuf 2020;6:101426. https://doi.org/10.1016/j.addma.2020.101426.
[10] Barba D, Alabort C, Tang YT, Viscasillas MJ, Reed RC, Alabort E. On the size and orientation effect in additive manufactured Ti-6Al-4V. Mater Des 2020;186:108235. https://doi.org/10.1016/j.matdes.2019.108235.
[11] Phutela C, Aboulkhair NT, Tuck CJ, Ashcroft I. The effects of feature sizes in selectively laser melted Ti-6Al-4V parts on the validity of optimised process parameters. Materials (Basel) 2020;13:117. https://doi.org/10.3390/ma13010117.
[12] Russell R, Wells D, Waller J, Poorganji B, Ott E, Nakagawa T, Sandoval H, Shamsaei N, Seifi M. Qualification and certification of metal additive manufactured hardware for aerospace applications. Addit Manuf Aerosp Ind 2019. https://doi.org/10.1016/b978-0-12-814062-8.00003-0.
[13] Yadollahi A, Shamsaei N. Additive manufacturing of fatigue resistant materials: Challenges and opportunities. Int J Fatigue 2017;98:14–31. https://doi.org/10.1016/j.ijfatigue.2017.01.001.
[14] Seifi M, Gorelik M, Waller J, Hrabe N, Shamsaei N, Daniewicz S, et al. Progress Towards Metal Additive Manufacturing Standardization to Support Qualification and Certification. JOM 2017;69:439–55. https://doi.org/10.1007/s11837-017-2265-2.
[15] Romano S, Miccoli S, Beretta S. A new FE post-processor for probabilistic fatigue assessment in the presence of defects and its application to AM parts. Int J Fatigue 2019;125:324–41. https://doi.org/10.1016/j.ijfatigue.2019.04.008.
[16] Romano S, Nezhadfar PD, Shamsaei N, Seifi M, Beretta S. High cycle fatigue behavior and life prediction for additively manufactured 17-4 PH stainless steel: Effect of sub-surface porosity and surface roughness. Theor Appl Fract Mech 2020:106. https://doi.org/10.1016/j.tafmec.2020.102477.
[17] Gong H, Rafi K, Gu H, Starr T, Stucker B. Analysis of defect generation in Ti-6Al-4V parts made using powder bed fusion additive manufacturing processes. Addit Manuf 2014;1:87–98. https://doi.org/10.1016/j.addma.2014.08.002.
[18] Li Y, Gu D. Parametric analysis of thermal behavior during selective laser melting additive manufacturing of aluminum alloy powder. Mater Des 2014;63:856–67. https://doi.org/10.1016/j.matdes.2014.07.006.
[19] Keshavarzkermani A, Marzbanrad E, Esmaeilizadeh R, Mahmoodkhani Y, Ali U, Enrique PD, et al. An investigation into the effect of process parameters on melt pool geometry, cell spacing, and grain refinement during laser powder bed fusion. Opt Laser Technol 2019. https://doi.org/10.1016/j.optlastec.2019.03.012.

[20] Cunningham R, Narra SP, Montgomery C, Beuth J, Rollett AD. Synchrotron-Based X-ray Microtomography Characterization of the Effect of Processing Variables on Porosity Formation in Laser Power-Bed Additive Manufacturing of Ti-6Al-4V. Jom 2017;69:479–84. https://doi.org/10.1007/s11837-016-2234-1.
[21] Shipley H, McDonnell D, Culleton M, Coull R, Lupoi R, O'Donnell G, et al. Optimisation of process parameters to address fundamental challenges during selective laser melting of Ti-6Al-4V: A review. Int J Mach Tools Manuf 2018. https://doi.org/10.1016/j.ijmachtools.2018.01.003.
[22] Mishurova T, Artzt K, Haubrich J, Requena G, Bruno G. New aspects about the search for the most relevant parameters optimizing SLM materials. Addit Manuf 2019;25:325–34. https://doi.org/10.1016/j.addma.2018.11.023.
[23] Mishurova T, Artzt K, Haubrich J, Requena G, Bruno G. Exploring the correlation between subsurface residual stresses and manufacturing parameters in laser powder bed fused ti-6al-4v. Metals (Basel) 2019;9. https://doi.org/10.3390/met9020261.
[24] Cunningham R, Zhao C, Parab N, Kantzos C, Pauza J, Fezzaa K, et al. Keyhole threshold and morphology in laser melting revealed by ultrahigh-speed x-ray imaging. Science (80-) 2019;363:849–52. https://doi.org/10.1126/science.aav4687.
[25] Gong H, Rafi K, Gu H, Janaki Ram GD, Starr T, Stucker B. Influence of defects on mechanical properties of Ti-6Al-4V components produced by selective laser melting and electron beam melting. Mater Des 2015;86:545–54. https://doi.org/10.1016/j.matdes.2015.07.147.
[26] Kasperovich G, Haubrich J, Gussone J, Requena G. Correlation between porosity and processing parameters in TiAl6V4 produced by selective laser melting. Mater Des 2016;105:160–70. https://doi.org/10.1016/j.matdes.2016.05.070.
[27] King WE, Barth HD, Castillo VM, Gallegos GF, Gibbs JW, Hahn DE, et al. Observation of keyhole-mode laser melting in laser powder-bed fusion additive manufacturing. J Mater Process Technol 2014;214:2915–25. https://doi.org/10.1016/j.jmatprotec.2014.06.005.
[28] Kamath C, El-Dasher B, Gallegos GF, King WE, Sisto A. Density of additively-manufactured, 316L SS parts using laser powder-bed fusion at powers up to 400 W. Int J Adv Manuf Technol 2014. https://doi.org/10.1007/s00170-014-5954-9.
[29] Scipioni Bertoli U, Wolfer AJ, Matthews MJ, Delplanque JPR, Schoenung JM. On the limitations of Volumetric Energy Density as a design parameter for Selective Laser Melting. Mater Des 2017. https://doi.org/10.1016/j.matdes.2016.10.037.
[30] Zhao C, Fezzaa K, Cunningham RW, Wen H, De Carlo F, Chen L, et al. Real-time monitoring of laser powder bed fusion process using high-speed X-ray imaging and diffraction. Sci Rep 2017. https://doi.org/10.1038/s41598-017-03761-2.
[31] Choo H, Sham KL, Bohling J, Ngo A, Xiao X, Ren Y, et al. Effect of laser power on defect, texture, and microstructure of a laser powder bed fusion processed 316L stainless steel. Mater Des 2019. https://doi.org/10.1016/j.matdes.2018.12.006.
[32] Makoana NW, Moller H, Burger H, Tlotleng M, Yadroitsev I. Evaluation of single tracks of 17–4PH steel manufactured at different power densities and scanning speeds by selective laser melting. South African J Ind Eng 2016;27:210–8. https://doi.org/10.7166/27-3-1668.
[33] Lykov PA. The energy density as a reliable parameter for characterization of selective laser melting of various alloys. Mater Sci Forum 2019;946 MSF:972–7. https://doi.org/10.4028/www.scientific.net/MSF.946.972.
[34] Caiazzo F, Alfieri V, Casalino G. On the Relevance of volumetric energy density in the investigation of inconel 718 laser powder bed fusion. Materials (Basel) 2020;13. https://doi.org/10.3390/ma13030538.
[35] Ghasemi-Tabasi H, Jhabvala J, Boillat E, Ivas T, Drissi-Daoudi R, Logé RE. An effective rule for translating optimal selective laser melting processing parameters from one material to another. Addit Manuf 2020;36:101496. https://doi.org/10.1016/j.addma.2020.101496.
[36] Rubenchik AM, King WE, Wu SS. Scaling laws for the additive manufacturing. J Mater Process Technol 2018;257:234–43. https://doi.org/10.1016/j.jmatprotec.2018.02.034.
[37] Torries B, Shamsaei N. Fatigue Behavior and Modeling of Additively Manufactured Ti-6Al-4V Including Interlayer Time Interval Effects. JOM 2017. https://doi.org/10.1007/s11837-017-2625-y.
[38] Soltani-Tehrani A, Pegues J, Shamsaei N. Fatigue behavior of additively manufactured 17–4 PH stainless steel: The effects of part location and powder re-use. Addit Manuf 2020;36:101398. https://doi.org/10.1016/j.addma.2020.101398.
[39] NASA. MSFC-SPEC-3717 - Specification for Control and Qualification of Laser Powder Bed Fusion Metallurgical Processes 2017:58. doi:MSFC-SPEC-3717.
[40] ASTM International. E606/E606M-12 Standard Test Method for Strain-Controlled Fatigue Testing. West Conshohocken, PA; ASTM Int 2012. doi:doi.org/10.1520/E0606_E0606M-12.
[41] Nezhadfar PD, Shrestha R, Phan N, Shamsaei N. Fatigue behavior of additively manufactured 17–4 PH stainless steel: Synergistic effects of surface roughness and heat treatment. Int J Fatigue 2019;124:188–204. https://doi.org/10.1016/j.ijfatigue.2019.02.039.
[42] Murakami Y. Metal Fatigue- Effects of Small Defects and Nonmetallic Inclusions; 2002. doi:10.4293/108680811X13125733356710.
[43] Manvatkar V, De A, DebRoy T. Spatial variation of melt pool geometry, peak temperature and solidification parameters during laser assisted additive manufacturing process. Mater Sci Technol (United Kingdom) 2015;31:924–30. https://doi.org/10.1179/1743284714Y.0000000701.
[44] Mukherjee T, Wei HL, De A, DebRoy T. Heat and fluid flow in additive manufacturing – Part II: Powder bed fusion of stainless steel, and titanium, nickel and aluminum base alloys. Comput Mater Sci 2018;150:369–80. https://doi.org/10.1016/j.commatsci.2018.04.027.
[45] Vecchiato FL, de Winton H, Hooper PA, Wenman MR. Melt pool microstructure and morphology from single exposures in laser powder bed fusion of 316L stainless steel. Addit Manuf 2020;36:101401. https://doi.org/10.1016/j.addma.2020.101401.
[46] Tang M, Pistorius PC, Beuth JL, Chris Pistorius P, Beuth JL, Pistorius PC, et al. Prediction of lack-of-fusion porosity for powder bed fusion. Addit Manuf 2017;14:39–48. https://doi.org/10.1016/j.addma.2016.12.001.
[47] Dai D, Gu D. Tailoring surface quality through mass and momentum transfer modeling using a volume of fluid method in selective laser melting of TiC/AlSi10Mg powder. Int J Mach Tools Manuf 2015;88:95–107. https://doi.org/10.1016/j.ijmachtools.2014.09.010.